International Journal of Fatigue 165 (2022) 107117

Contents lists available at ScienceDirect

International Journal of Fatigue

journal homepage: www.elsevier.com/locate/ijfatigue

Directions of high cycle fatigue cracks emanating from circular notches studied by optical profilometry

J.A. Balbín [a,b,*], V. Chaves [a], N.O. Larrosa [a,c], C. Madrigal [a], A. Navarro [a]

[a] Departamento de Ingeniería Mecánica y Fabricación, Escuela Técnica Superior de Ingeniería, Universidad de Sevilla, Camino de los Descubrimientos s/n, 41092 Sevilla, Spain

[b] Departamento de Ingeniería Minera, Mecánica, Energética y de la Construcción, Escuela Técnica Superior de Ingeniería, Universidad de Huelva, Campus Universitario de El Carmen, 21007 Huelva, Spain

[c] Department of Mechanical Engineering, University of Bristol, Bristol BS8 1TR, England, United Kingdom

ARTICLE INFO

Keywords:
High cycle fatigue
Notch
Crack path
Crack initiation point
Crack direction

ABSTRACT

Current models for predicting the fatigue endurance of notched solids use the stresses along a straight line, beginning at the notch root, as a simplification of the real crack propagation path. In this work, the experimental crack paths for hollow notched samples were analysed through different microscopy techniques, with the objective of establishing high cycle fatigue crack growth directions in a mild steel. Fully reversed tension–compression fatigue tests ($R = -1$) of thin-walled tube specimens with a passing-through hole were carried out. The crack paths observed in the outer cylindrical surface were studied in each case, with special attention to the crack initiation point and the crack direction along the first grains. Moreover, the analysis of the fracture surfaces allowed the same analysis to be performed to determine the internal crack paths. It was observed that the crack initiation point was close to the maximum principal stress point at the hole contour as obtained from linear elastic finite element analysis, and the crack direction in its initiation was generally close to Mode I direction, contrary to the conventionally accepted 45° crack growth direction.

1. Introduction

In polycrystalline materials, such as metals, fatigue crack initiation generally occurs near the plane of maximum shear stress, i.e. in the mode II direction, and then crack propagation carries on near the plane perpendicular to the maximum tensile stress, i.e. in the mode I direction. These two phases of crack growth are commonly referred to as stage I and stage II of fatigue crack growth, respectively, which were analysed in depth by Forsyth [1,2]. In [1], Forsyth shows an excellent photograph for a pure cold rolled aluminium alloy, in which these two phases are clearly observed. The stage I to stage II transition is not yet well established. According to Forsyth, stage I ceases when the crack meets a slip obstacle such as a grain boundary, so the crack commonly changes to normal growth when the tip of the crack reaches the first grain boundary [1]. Miller indicates that the transition occurs usually at a crack depth of 3-to-5 grains [3]. However, reality does not seem so simple: Forsyth himself indicates that fractographic evidences suggest that during stage I the crack may deviate from the maximum shear plane, following structural inhomogeneities [2], and that under certain conditions, stage I may not occur in a detectable way, as it happened with an aluminium–zinc–magnesium alloy, in which the iron aluminide particles inhibited the sliding of dislocations and caused the crack not to start at 45° but normal to the tensile stress [1].

The presence of a notch, characterised by a high stress region close to the notch root, from where the crack generally initiates, might modify stages I and II of fatigue crack growth. According to Forsyth, the combined effect of a notch and high mean stress usually encourages stage II, with no presence of stage I [2]. There are several experimental studies in the literature about the crack propagation direction during the initial period of crack growth in notched solids, and they are inconclusive: Frost studied non-propagating cracks from circumferential sharp V-notches in cylindrical specimens under reversed axial and rotating bending loading [4,5] for mild steel and aluminium alloy. Unbroken specimens were sectioned in the longitudinal direction and the non-propagating cracks were examined at the notch root with an optical microscope. Of the 19 cracks analysed and shown in the tables and figures of these articles, most were formed at 90° with respect to the load direction, that is, in the mode I direction, typical of stage II. Although there were also several cracks that were formed at 45°

* Corresponding author at: Departamento de Ingeniería Mecánica y Fabricación, Escuela Técnica Superior de Ingeniería, Universidad de Sevilla, Camino de los Descubrimientos s/n, 41092 Sevilla, Spain.
E-mail address: jbalbin@us.es (J.A. Balbín).

https://doi.org/10.1016/j.ijfatigue.2022.107117
Received 1 April 2022; Received in revised form 14 June 2022; Accepted 30 June 2022
Available online 13 July 2022

(in mode II), 2 at 120° and 1 at 30°. Meneghetti et al. studied low carbon steel plates weakened by U-notches [6]. The specimens were tested under axial cyclic loading and the crack paths were inspected with a microscope on the two surfaces of each specimen. The angle of crack initiation, measured with respect to the notch bisector, ranged from 16° to 30° and the average value was equal to about 25°. Tanaka et al. studied thin-walled tubular specimens of medium-carbon steel with a hole drilled in the middle of the specimen, subject to in-phase and out-of-phase combinations of cyclic torsion and axial loadings [7]. The cracks, observed with an optical microscope on the specimen surface, propagated almost straight for all cases examined. Berto et al. [8] tested circumferentially V-notched specimens made of hardened and tempered steel. As in the case of Frost, some run-out specimens were sectioned in the longitudinal direction and the paths of non-propagating cracks were examined. As seen in two pictures of the article, for two axial load tests, the cracks had approximately the mode I direction from their beginning. Gates and Fatemi conducted multiaxial fatigue tests on thin-walled aluminium tubular specimens with a circular transverse hole and observed cracks on the specimen surface with an optical microscope [9]. The cracks nucleated and grew on planes of maximum shear for, at least, 100 μm before turning to grow on the maximum principal stress plane. Lorenzino and Navarro tested Al1050 aluminium alloy plates with a circular hole under axial loading [10]. The material had a large grain size, with the notch size of the same order or even smaller than the grain size. They studied the cracks growing from the hole on the two specimen surfaces with two optical microscopes and found that the crack paths were very irregular in their initial part, corresponding to the first grains, being highly affected by the microstructure of the material. Based on all these results from the literature, it is difficult to establish what stages I and II are like in notches, with cases of cracks growing from the beginning in mode I, others with cracks initiating in mode II, and a few cases with cracks initiating in mixed mode direction. This may be just as well, for this great experimental diversity of stage I directions from notches could justify the use of very different crack paths in current notch multiaxial fatigue limit models: mode I direction [11], mode II direction [12] or a mixed-mode direction [13–15].

In addition, these experimental studies from the literature analysed the crack initiation direction on the external surface of the specimens [6,7,9,10] and, in the case of the works by Frost [4,5] and Berto et al. [8], in a longitudinal section of the cylindrical specimens. However, it is likely that the crack started somewhere inside the specimen and not on the external surface or, in the case of the specimens analysed by Frost and Berto et al. in a different section from the one studied. This implies that the directions studied in these works [4–10] may not be exactly representative of the crack initiation directions as the cracks could have initiated in a plane different from the studied ones. In recent years, there has been a great advance in the field of microscopy. Specifically, 3D profilometers have been developed, which allow the determination of the surface topography. This type of equipment has been used in a recent experimental campaign to analyse the fracture surfaces of notched specimens subjected to cyclic loading and to record the evolution of the crack direction in the internal planes of the specimens, and not only in the plane of the external surface of the specimen. It allows a more precise knowledge of stages I and II of fatigue crack growth from notches. This experimental campaign began with a study on AISI 304L stainless specimens [16] and continued with 7075 aluminium alloy specimens [17]. The present document reports the experimental study on a third material, a mild steel. The geometry was a thin-walled tube with a passing-through hole under axial loading. The crack paths were studied on the external surface of the specimen and also on the fracture surfaces. The results of the present research can lead to a better understanding of the crack paths in notches and to a better selection of the crack lines in notched fatigue limit models so that they are truly representative of the experimental crack paths.

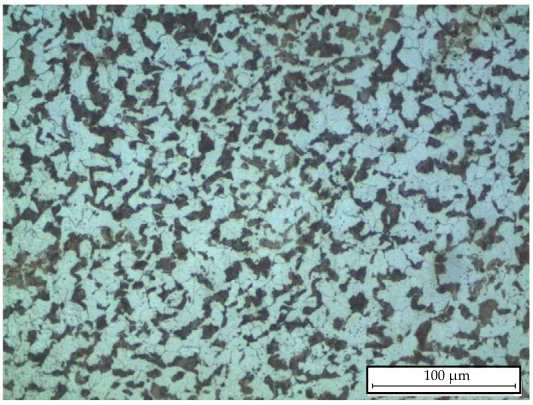

Fig. 1. Granulometry of S355 low carbon steel.

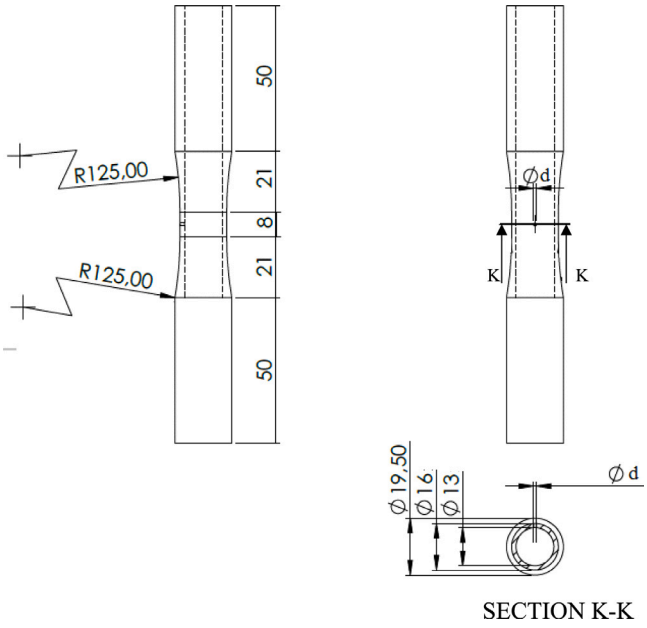

Fig. 2. Geometry of the notched specimen.

2. Material and tests

The material used in this work is commercial low carbon S355 steel (also known as St52). Its chemical composition (weight %) is: 0.18 C, Mn 1.28, Si 0.30, P 0.03, S 0.02, Cr 0.18, Ni 0.06, Al 0.025, Mo 0.01. The average grain size is 33 μm (see Fig. 1). No heat treatment was applied after the machining of the specimens. The monotonic properties, as determined from 20 tensile tests, are as follows: tensile strength σ_{UTS} = 586 MPa, yield strength σ_{YS} = 412 MPa, Young's Modulus E = 208 GPa. Vickers hardness equals to 187.9 HV. This material combines good fatigue behaviour with low environmental impact for non-transport applications [18].

Firstly, fatigue tests under fully-reversed axial loading ($R = -1$) were conducted on smooth cylindrical specimens in a servo-hydraulic axial load frame at 6–8 Hz. Then, notched specimens were manufactured for fatigue tests. The geometry of the notched specimen was a thin-walled tube of 1.5 mm thickness with a passing-through hole in the central section. Three different hole diameters d = 0.8, 1.5 and 3.4 mm were done, in order to check whether there was a hole size effect on the experimental crack paths or not. As for the smallest hole size, a diameter d = 0.8 mm was chosen. This diameter fulfilled the basic desired conditions: to be machined with a conventional drilling

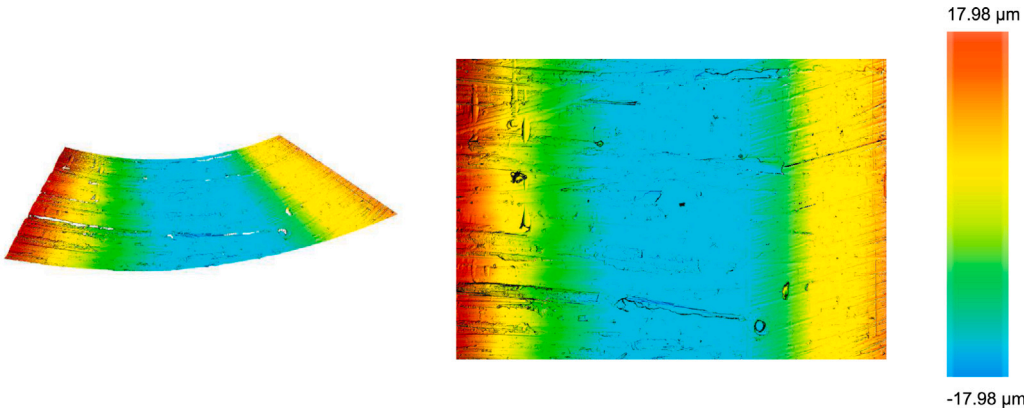

Fig. 3. Example of 3D captured hole surface from which surface roughness was measured.

machine and to meet the tolerances proposed in the drawings. Regarding the largest size, its choice was based on achieving a geometry which had an elastic stress field in a plane perpendicular to the hole similar to that of an infinite plate with a hole of the same size. This would greatly facilitate future parametric predictions with multiaxial notch fatigue models, as the Kirsch's equations [19, p. 91] could be used. It is the effect of the curvature of the cylinder that makes the stress field in the vicinity of the hole different from that of a hole in an infinite plate. Although if the cylinder is large enough and the transverse circular hole is small enough, then the difference in stresses in both cases becomes very small. For the cylindrical specimens tested in the present work, with an outside diameter of 16 mm, elastic studies for axial, torsional and biaxial loads ($\sigma_y^\infty = \tau^\infty$) indicated that for a circular hole with a diameter not greater than 3.5 mm, the stress gradient ahead of the hole was very similar to the case of an infinite plate with a hole, the difference in K_t being less than 5% [20]. As a result, a maximum hole diameter of 3.4 mm was chosen to achieve a similar stress field to that in the infinite plate configuration. Finally we chose an intermediate diameter of 1.5 mm.

Fig. 2 shows the geometry of the specimen. These notched specimens were tested in a resonance fatigue testing machine, at approximately 150 Hz for fully-reversed axial loading ($R = -1$). Surface roughness measurements were taken at the drilled hole to assess the surface finishing of this stress concentrator element. A noncontact 3D optical profilometer was used. First, the internal surface of the hole was captured (see Fig. 3), and then a Gaussian filter was applied. After that, the curved surface was adjusted to remove the inclination and to obtain a levelled surface. Three specimens were chosen from each of the hole sizes $d = 0.8$ mm and $d = 1.5$ mm and three roughness measurements were taken at the bottom of the hole on each sample. Values of mean roughness for the area of the captured surface, R_a, root mean square roughness, R_q, and maximum roughness, R_z, were obtained as indicated in ISO 25 178. Mean roughness and maximum roughness presented an average value of 0.66 µm and 9.49 µm, respectively.

3. Experimental results

Fatigue tests results were used to construct the S-N curves in accordance with ASTM E739 [21], assuming a linear relationship between the variables $log(\sigma)$ and $log(N)$. Fatigue tests results are plotted in Fig. 4 where stress values are referred to the net section. Hollow circles refer to broken specimens and solid squares refer to run-out tests. The stress is expressed in terms of stress amplitude, calculated by the expression $\sigma = F/s$, where F is the applied force amplitude and s is the area of the cross section of the notched hollow specimen. All S-N curves shown in Fig. 4 have the same scale in order to be able to clearly appreciate the differences among cases. Tables summarising the tests loadings and fatigue lives are given in Appendix A. As expected, Fig. 4 shows that the S-N curve for the smooth specimen is above the curves for the notched specimens, and with respect to the notched specimens, the curves for those with a smaller diameter are above the ones for those with a larger diameter. As a matter of fact, the endurance limit at 10^6 cycles was $\sigma = 275$ MPa for the smooth specimen and $\sigma = 175$, 152, 138 MPa for the notched specimens with $d = 0.8$, 1.5 and 3.4 mm, respectively.

4. External crack paths

In this work, special attention has been paid to the crack initiation location and the crack direction path, especially during the first period of crack growth, as some models base their evaluations on stresses along a line that is supposed to be representative of the crack path. This work deals with the experimental measurement of the crack initiation point and the crack direction not only at the external surface of the specimen but also at the specimen's internal planes. Measurements of the angle of the crack initiation point and crack direction have been performed only in specimens falling in the high cycle fatigue regime, that is, specimens broken beyond 10^5 cycles.

Fig. 5 shows the axis layout reference framework used, where the origin of the coordinate system $OXYZ$ is located on the specimen's external surface in the centre of the hole. The X-axis is in the central transverse section of the specimen, the Y-axis runs along the longitudinal dimension of the specimen and the Z-axis coincides with the axis of the hole. The location of the crack initiation point at the hole contour and the crack direction at some specific distances from the crack initiation point are indicated by the angles θ and θ_1, respectively, whose geometrical definition is sketched in Fig. 6. Angles are measured counterclockwise. The crack initiation point angle θ is defined as $\tan^{-1}(\Delta Y)/(\Delta X)$. The crack direction angle θ_1 is measured using an additional coordinate system $o'x'y'$ whose origin coincides with the crack initiation point at the hole contour. The angle θ_1 is defined as $\tan^{-1}(\Delta y')/(\Delta x')$. This crack direction angle θ_1 has been studied at several crack lengths, $a \approx \sqrt{(\Delta x')^2 + (\Delta y')^2}$, equal to some multiples of the averaged grain size, D, and also to some values based on the El-Haddad short-crack parameter L [22], that is 1, 2, 5, 10, 15 and 20 grains, and also $L/2$, L and $2L$. The reason is that several well-known notched fatigue models based their estimations on the elastic stresses calculated on lines whose lengths are multiples of the grain size D, such as the Navarro–Rios model [23], and lengths that are based on the parameter L, such as Taylor's Point and Line Methods [12]. In this work, a value of $L = 158$ µm was estimated for the studied material through the value of K_{th} obtained using the microstructural equation for the Kitagawa–Takahashi diagram $D = \frac{2}{\pi}\left(\frac{K_{th}}{\sigma_{FL}}\right)^2\left(\frac{m_1^*}{m_\infty^*}\right)^2$ (see [24]), where m_1^* is the grain orientation factor when the crack spans a single grain, K_{th} is the fatigue stress intensity factor threshold, σ_{FL} is the plain fatigue limit, and the term m_∞^* is the orientation factor for truly polycrystalline behaviour when the crack is large enough to span

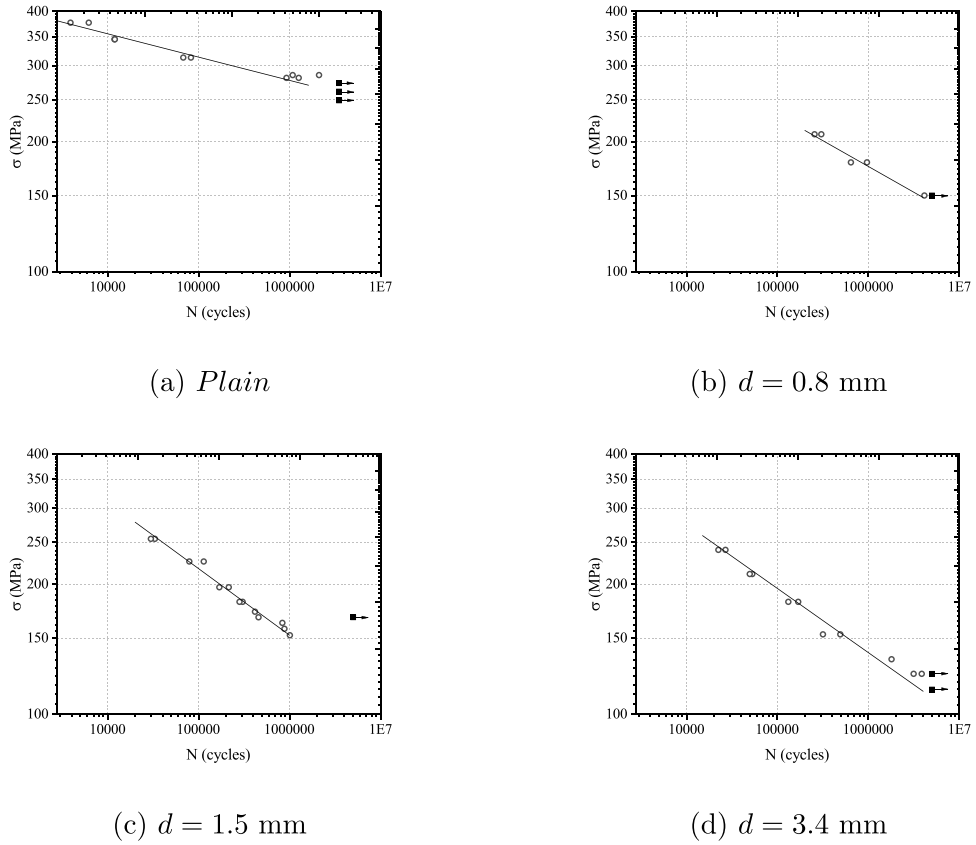

Fig. 4. Fatigue tests conducted on S355 steel specimens.

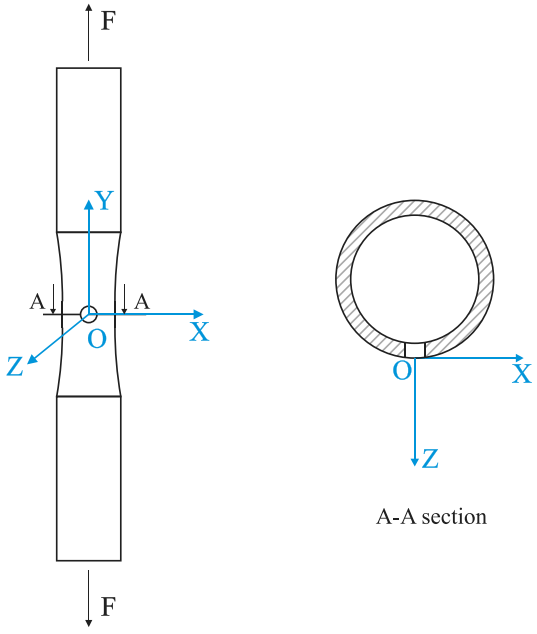

Fig. 5. Axes layout.

several grains. Tables summarising crack initiation point angles (θ) and crack direction angles (θ_1) for the several crack lengths measured are given in Appendices B and C.

Regarding the crack at the external surface of the specimen (Z = 0, data included in Appendix B and Table C.1 of Appendix C), a total of 22 specimens have been analysed for the three circular notch

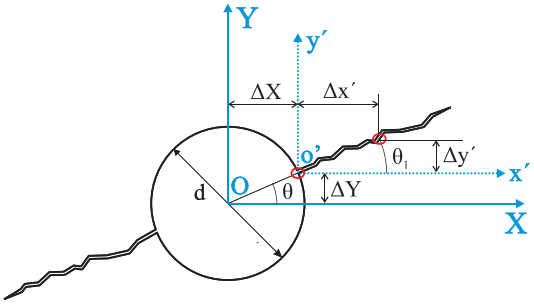

Fig. 6. Scheme of crack initiation point and crack direction angles.

diameters, with two opposite cracks emerging from the hole in all cases. Fig. 7 shows two cases of the experimental measurement of the crack initiation point. Crack initiation point angles in Fig. 7a are close to zero, that is, $\theta = -3.9°$ for the crack growing in the left side of the hole ($X < 0$), and $\theta = -1.8°$ for the crack growing in the right side of the hole ($X > 0$). Likewise, Fig. 7b also shows angles close to zero, that is, $\theta = 0.7°$ ($X < 0$) and $\theta = -5.8°$ ($X > 0$).

In the same way, Fig. 8 shows how the crack direction angle θ_1 was measured in two different specimens ($X > 0$). In Fig. 8a, angle $\theta_1 = -19.4°$ is found for a crack length of two averaged grain sizes, and in Fig. 8b angle $\theta_1 = -0.2°$ is found for a crack length of five averaged grain sizes.

Once all external cracks were evaluated, the analysis was made using the absolute values of the θ and θ_1 angles, to prevent positive and negative values from cancelling each other when averaging results. Thus, the crack initiation point angle, θ, presented a average value of 4.2° with an standard deviation of 2.7°. That is, the crack initiation point is close to the maximum principal stress point at the hole contour

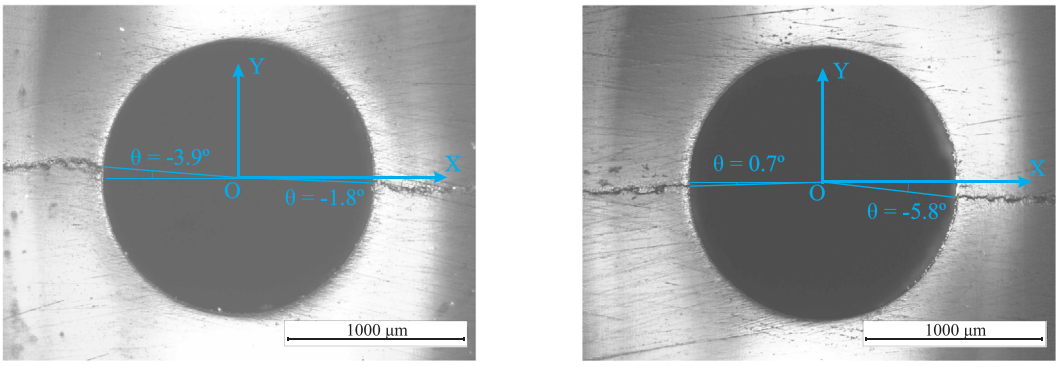

(a) N = 304400 cycles (b) N = 415900 cycles

Fig. 7. Crack initiation point angles, θ, measured over the external surface of the specimen.

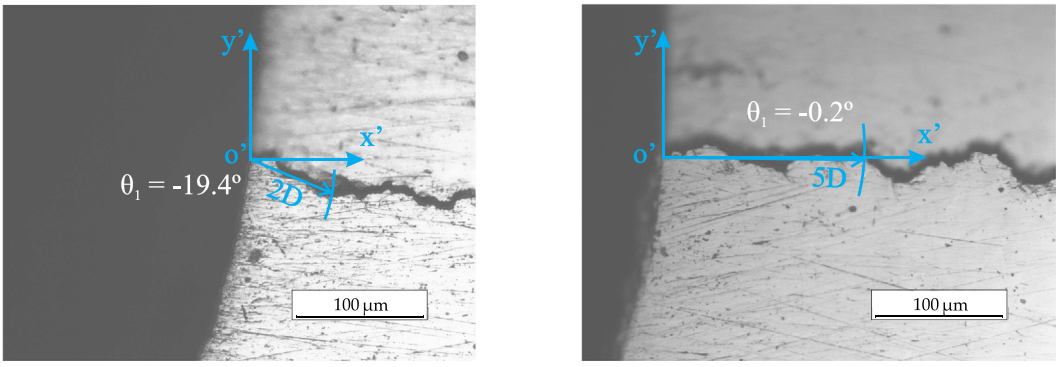

(a) N = 455500 cycles (b) N = 415900 cycles

Fig. 8. Crack direction angles, θ_1, measured over the external surface of the specimen.

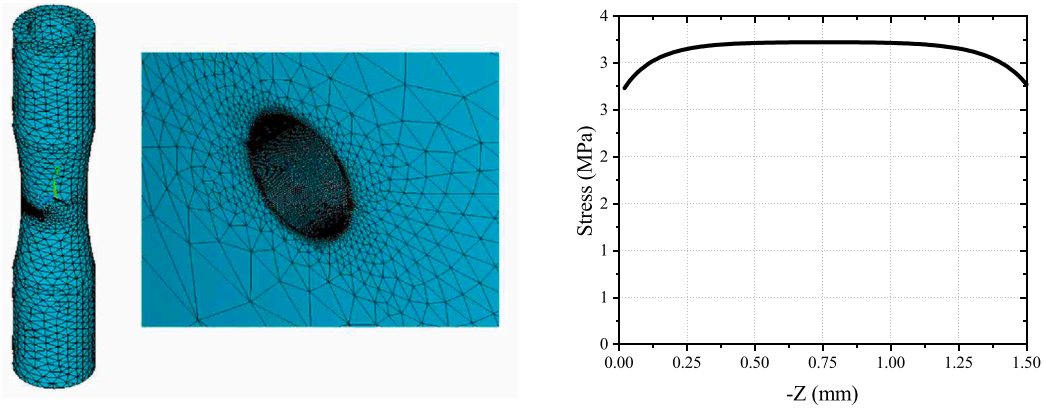

a) b)

Fig. 9. (a) Specimen model and mesh used in FEM analysis. Detail of the mesh around the hole. (b) First principal stress S_{11} along the 1500 µm hole depth (line $X = d/2$) for axial loading and $d = 1$ mm.

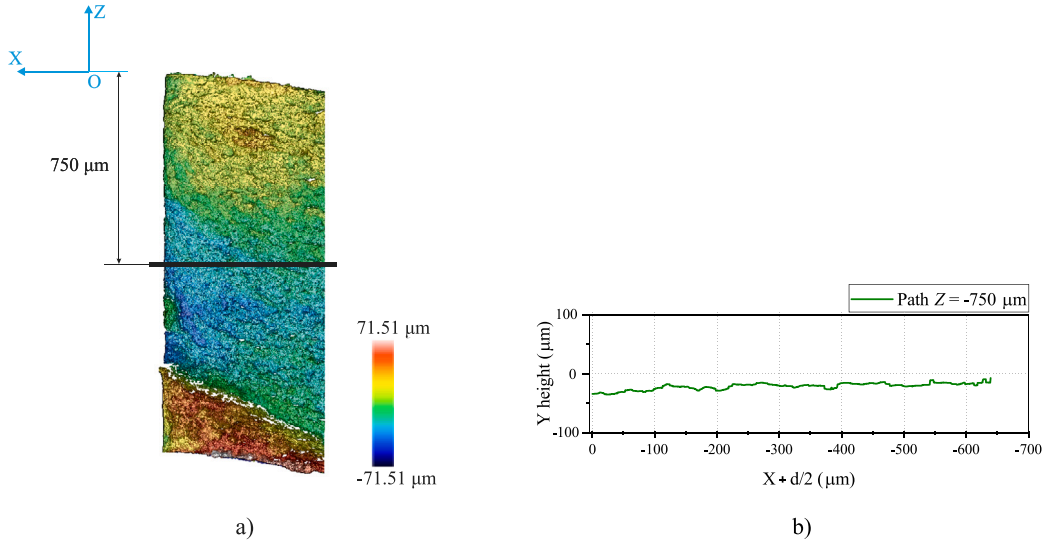

Fig. 10. (a) Fracture surface and mid-thickness plane ($Z = -750$ µm) and (b) heights of the crack path points. (For interpretation of the references to colour in this figure legend, the reader is referred to the web version of this article.)

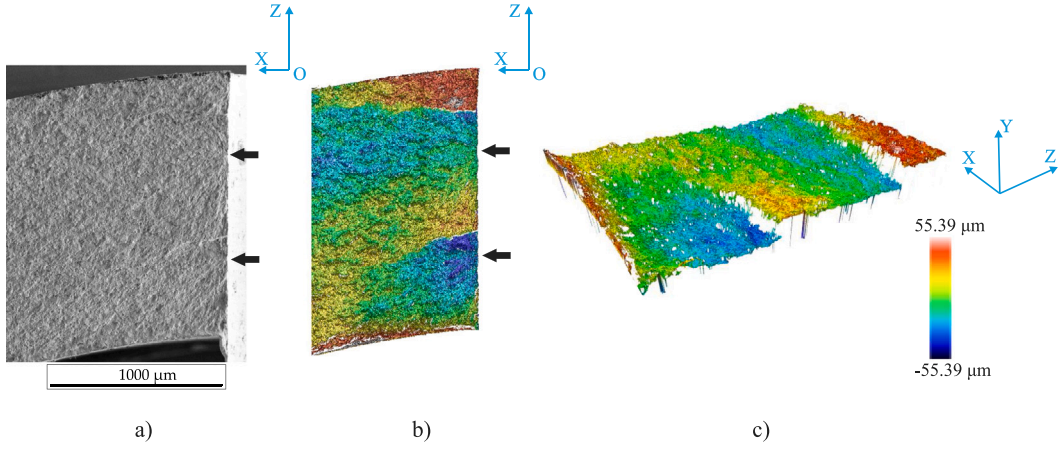

Fig. 11. (a) SEM (b) 2D profile (OP) and (c) 3D profile (OP) fractographs of a fracture surface. Specimen broken after 169 000 cycles and hole diameter $d = 1.50$ mm. (For interpretation of the references to colour in this figure legend, the reader is referred to the web version of this article.)

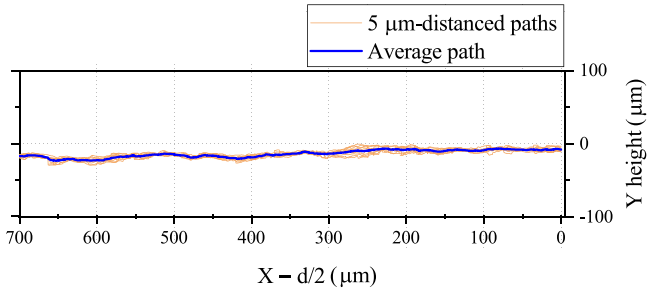

Fig. 12. Average path at $Z = -478$ µm. Specimen broken after 169 000 cycles. (For interpretation of the references to colour in this figure legend, the reader is referred to the web version of this article.)

($\theta = 0°$). Similarly, an average crack direction angle of $\theta_1 = 21.8°$ was found for a crack length of one averaged grain size, $1D$, and a $\theta_1 = 14.7°$ angle for a crack length of two averaged grain sizes, $2D$. Furthermore, this crack direction angle θ_1 presented an average value of 9.4° for a crack length of $L/2$, and 6.0° angle for a crack length of L. These values certainly differ from Mode I and Mode II directions. However, the crack direction angles measured at larger crack lengths approach the Mode I direction.

5. Crack path analysis on the fracture surfaces

In a previous work [17], the point of maximum principal stress of a whole specimen, similar to those tested in this work, was calculated through a finite element analysis (commercial software ANSYS v15.0 [25]). SOLID187 elements, which are 10-node and 3D tethrahedral structural solid elements, and different mesh sizes were used in a linear elastic analysis. The models were re-meshed to ensure that the difference between the stresses of a model and the previous one were practically negligible. The final mesh had an element size of approximately 2 mm, being refined at the hole area, up to an element size of 0.025 mm. Fig. 9a shows the model geometry and mesh, and the detail of the mesh around the hole, for a $d = 1$ mm case. As for the

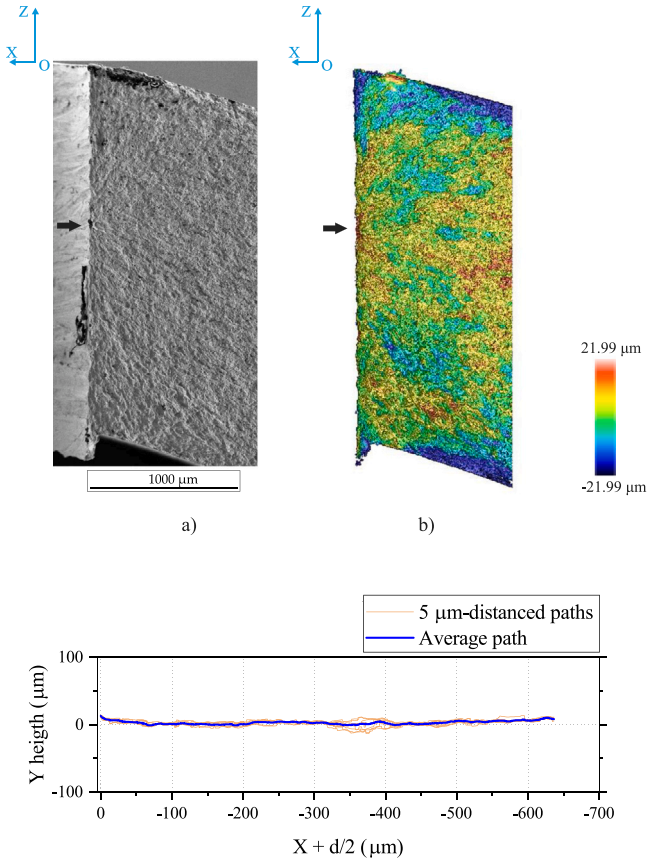

Fig. 13. (a) SEM and (b) 2D profile (OP) fractographs of a fracture surface. (c) Average path at $Z = -649$ µm. Specimen broken after 315 600 cycles and hole diameter $d = 3.40$ mm. (For interpretation of the references to colour in this figure legend, the reader is referred to the web version of this article.)

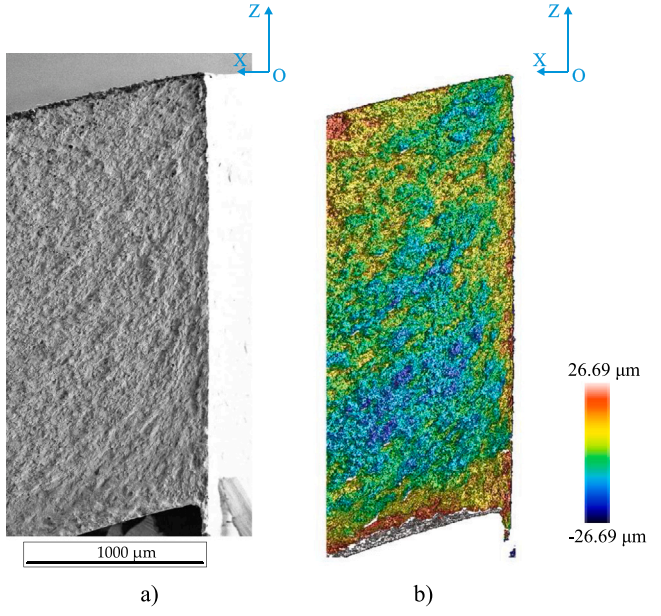

Fig. 14. (a) SEM and (b) 2D profile (OP) fractographs of a fracture surface. Specimen broken after 491 200 cycles. (For interpretation of the references to colour in this figure legend, the reader is referred to the web version of this article.)

boundary conditions, the specimen was clamped at the bottom surface and a unitary stress was applied on the upper surface. Fig. 9b shows the maximum principal stress S_{11} along the line $X = d/2 = 0.5$ mm, i.e. the line at the hole surface at $\theta = 0°$, where the maximum principal stress is located. This line has the length of the hole, i.e., 1500 µm. As a result of the low out-of-plane constraint conditions at the sample surface (i.e. reduced stress triaxiality), the maximum principal stress point is not located at the external surface ($Z = 0$) but at $Z = -750$ µm, i.e., at the mid-thickness plane of the specimen. However, the stress profile is pretty flat in the central part of the hole.

Because of that, the crack initiation point and the crack direction were subsequently evaluated at this $Z = -750$ µm internal plane, assuming that this would be the most likely plane in which fatigue crack initiation would occur. To do that, an analysis of the fracture surfaces at both sides of the hole was carried out using an optical microscope, a scanning electron microscope (SEM) and a noncontact 3D optical profilometer (OP). The 3D topography of the fracture surfaces was captured using the OP through the Focus Variation technology, which is useful for measuring the shape of large rough surfaces. It also allows measurements including high slope surfaces (up to 86°), high measurement speed and large vertical range. The resolution is half a micron in the three coordinate axes.

An example of the fracture surface captured with the OP is presented in Fig. 10a. Only one of the two fracture surfaces generated from the hole is shown, in this case the one located at $X < 0$ (following the coordinate system defined in Fig. 5). The points of the fracture surface with higher Y values are shown in red, blue points refer to lower Y values and white areas indicate steep slope. The intersection of the fracture surface with the mid-thickness plane ($Z = -750$ µm) results on the mid-thickness crack path shown in Fig. 10b, plotted as a solid black line in Fig. 10a. The path in the mid-thickness plane has a similar trend to the path studied on the outer surface, that is, the initiation point (at $X + d/2 = 0$ µm) is close to the point of maximum principal stress and the direction of the crack is close to Mode I (horizontal direction) from the initiation. The angle θ measured on the external surface of the specimen ($Z = 0$) serves as the reference to obtain the value of this angle θ in the $Z = -750$ µm crack path. This calculation consists on a relation between the Y heights of the crack initiation point at $Z = 0$ and the crack initiation point at $Z = -750$ µm. The average value of the angle θ for all the $Z = -750$ µm crack paths was 4.9°, which is very similar to average value 4.2° reached on the external surface of the specimen ($Z = 0$). For the $Z = -750$ µm crack path, an average crack direction angle of $\theta_1 = 14.2°$ was found for a crack length of one averaged grain size, $1D$, and a $\theta_1 = 9.0°$ angle for a crack length of two averaged grain sizes, $2D$. These values also differ from Mode II direction. Crack direction angles measured at larger crack lengths approach to Mode I direction again. An example is a $\theta_1 = 2.5°$ angle obtained for a crack length of ten averaged grain sizes, $10D$.

A more careful analysis of the fracture surfaces showed that the cracks did not initiate exactly from the mid-thickness plane ($Z = -750$ µm). Radial lines pointing to the origin of the crack were observed in the SEM and OP fractographs, indicating that the cracks' origins were scattered along the central segment of the hole. The most likely reason for this large variability in the initiation point location may be the low variation of the maximum stress throughout the 1500 µm depth of the hole. The first principal stress profile shown in Fig. 9b indicates that its value changes very little over the 1500 µm studied, except for the two end zones, corresponding to the external and internal surface of the hollow specimen. Hence, if cracks usually initiate from the point where the maximum principal stress is reached and it remains almost constant in the studied case, the cracks could randomly initiate at any location within this region that is, the cracks could have initiated from almost any Z point along the planes $X = \pm d/2$ and not exactly from the mid-thickness plane ($Z = -750$ µm). For this reason, the fracture surfaces were carefully analysed with the SEM and OP equipments, trying to

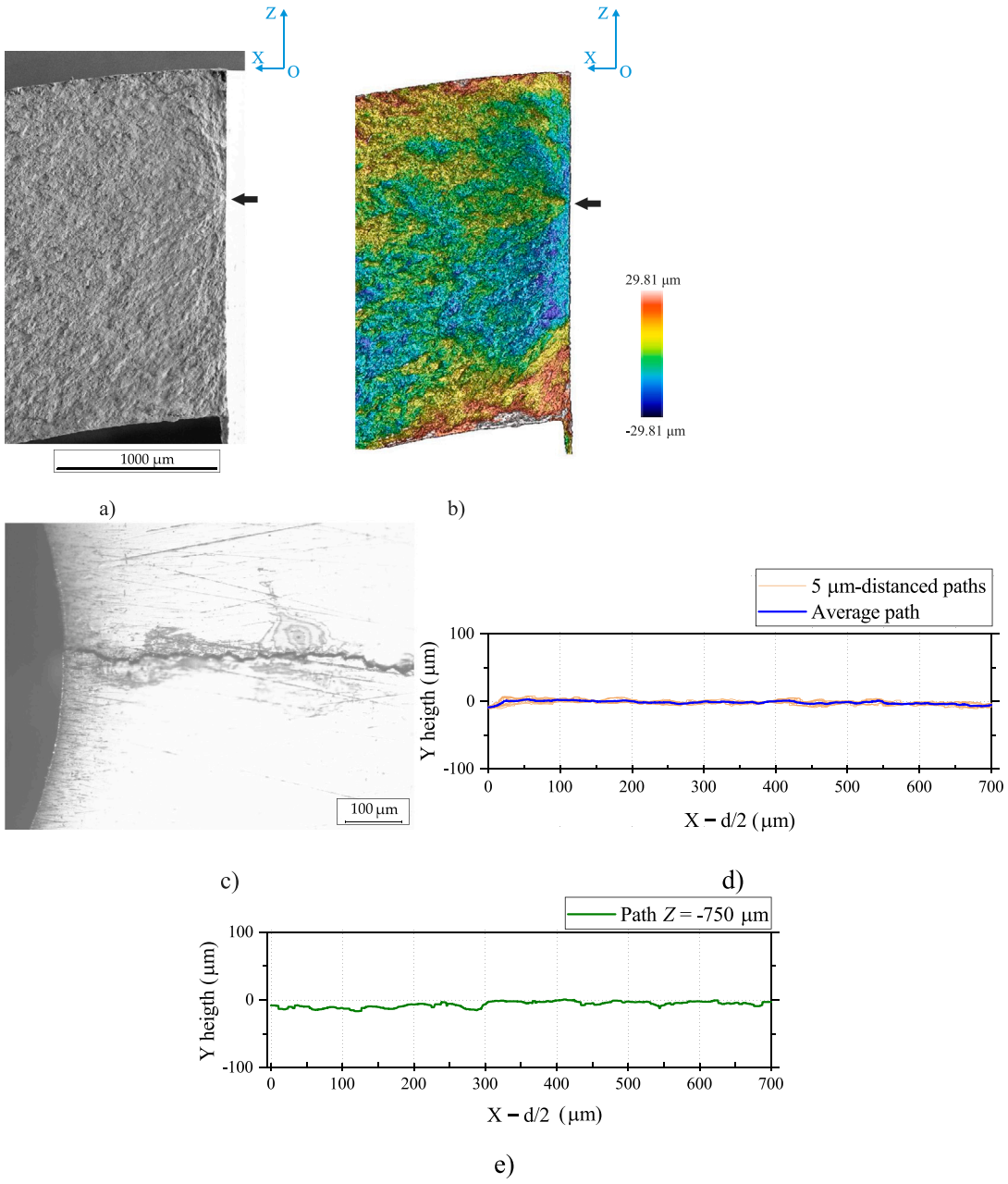

Fig. 15. (a) SEM, (b) 2D profile fractographs of a fracture surface, (c) External crack path ($Z = 0$), (d) Average path around the initiation point and (e) midplane thickness crack path ($Z = -750$ µm). Specimen broken after 831 100 cycles. (For interpretation of the references to colour in this figure legend, the reader is referred to the web version of this article.)

locate the fatigue cracks and their initiation points, to subsequently study the corresponding crack paths.

Fig. 11 shows the fractographic examination of a fracture surface ($X > 0$). The SEM and 2D/3D topography captured profiles (OP) are provided. In all these fractographic images, several planes are observed that probably correspond to different cracks. The smooth fatigue surface crosses the entire thickness of the specimen, i.e. 1500 µm. Paying attention to the area adjacent to the hole, three macrocracks are observed, which in the OP fractographs correspond to three zones of different colour: red–orange, blue–green–yellow and blue areas observed in the downward direction. Each of these macrocracks are relatively horizontal, although located at different Y heights, then connecting abruptly where they meet, as can be seen in the 3D fractography. The two areas of abrupt connection are in white, corresponding to zones of steep slope. Ratchet marks when the three cracks intersects, can also be seen in the SEM picture. Radial lines pointing to the crack initiation zone can be observed in the SEM and OP fractographs. The initiation zones of two of the three cracks are indicated with black arrows, none of them located in the mid-thickness plane ($Z = -750$ µm). The possible crack initiations are located around $Z = -478$ µm and $Z = -1078$ µm in this case.

The crack paths corresponding to the planes where each crack initiated were studied. As it was not possible to locate the exact initiation points of the cracks, but rather an initiation zone, which was estimated to be 50 µm in size, paths in several parallel planes at a

Table 1
Crack initiation point angle, θ, and crack direction angle, θ_1, for specimen broken at 831 100 cycles, showed in Fig. 15.

Crack path location	θ	θ_1			
		1D	2D	L/2	2L
External surface $Z = 0$ μm	3.6°	14.1°	−0.6°	−10.0°	−2.8°
Mid-thickness plane $Z = -750$ μm	−5.8°	−18.1°	−1.9°	−2.4°	1.6°
Localised crack initiation $Z = -559$ μm	−5.9°	16.6°	12.8°	7.1°	1.4°

distance of $Z = 5$ μm from each other, and sweeping the 50 μm of the initiation zone, were studied. Thus, 11 parallel paths were studied for each initiation zone. Fig. 12 shows the heights of these 11 paths for the crack that starts at $Z = -478$ μm located on the specimen shown in previous Fig. 11. It is observed that the Y heights of these paths run approximately parallel to each other. The average path of these 11 paths, shown in blue colour, was taken as representative of the path of this crack. It is observed that the direction of this average path is very close to 0°, even at the initial period of crack growth, contrary to the commonly assumed 45° crack initiation direction, which would correspond to Mode II direction. The crack paths have been only evaluated along a 700 μm length since this distance approximately represents a crack that spans twenty grains of the material used in this work.

In contrast to what has just been described, other surfaces analysed show a single plane with a main crack occupying a large area of the specimen's section, as represented in (a) SEM and (b) OP fractographs included in Fig. 13. In this case ($X < 0$), the yellow area is predominant over almost the entire surface and the crack initiation could be located at approximately where the black arrow is placed ($Z = -649$ μm), that is the red little area adjacent to the hole to which the radial lines converge. Furthermore, a mixed-Mode crack initiation is observed in its corresponding average path, included in Fig. 13c. In this average path, the crack direction angle is $\theta_1 = 21.8°$ for a crack length of one averaged grain size and $\theta_1 = 10.8°$ for a crack length of two averaged grain sizes. A total of ten clearly detectable crack initiation locations were observed among all the fracture surfaces analysed microscopically.

Additionally, other cases have been observed where the fracture surface seems to be uniform but no clear crack initiation is visible. An example of this situation is shown in Fig. 14, where an almost homogeneous fracture surface is observed. The area adjacent to the hole is practically red–yellow coloured and almost the entire blue surface indicates that is a uniform surface. A possible explanation for not finding a clear crack initiation location is that a large number of small cracks might be initiated in different locations.

To make a final analysis of the results obtained, a comparison between the external path ($Z = 0$), the mid-thickness plane path ($Z = -750$ μm) and the localised crack initiation average path ($Z = -559$ μm) is done, all corresponding to the fracture surface presented in Fig. 15 which belongs to a specimen broken after 831 100 cycles and hole diameter $d = 1.50$ mm. Please note that in the plotted paths, the X-axis has been reversed. As can be seen, there are clear differences among the crack paths in this case. The external crack path initiates almost horizontally and just then decreases slightly in contrast to average path $Z = -559$ μm which shows a clear mixed-Mode crack direction at the beginning and then stays approximately horizontal. However, the three paths continue horizontally at larger crack lengths. The $Z = -750$ μm path seems to be almost horizontal for the whole plotted path. These differences are more noticeable in Table 1 where a brief summary of the angles θ and θ_1 are provided for the three crack paths of this case. For the sake of simplicity to make the comparison, the real angle values are provided instead of absolute values. It is observed that the external crack path might not be representative of the crack which grows inside.

As a summary, Table 2 shows the average values of angles θ and θ_1 measured at different locations of the crack path for all the evaluated specimens in the present work. In addition, standard deviation values are included in parentheses. This Table 2 includes data obtained from the 22 fatigue-tested specimens broken beyond 10^5 cycles. The crack initiation point is close to the maximum principal stress point ($\theta = 0°$) since θ angle does not exceed the value of six degrees in the three analysed locations of the crack path. In general, the crack direction angles θ_1 indicate that mixed-Mode direction is found at the initial period of crack growth on the external surface of the specimen ($Z = 0$) as it is close to nineteen degrees. Regarding the crack initiations that could be located on the fracture surfaces, the average path indicates that the crack direction is close to Mode I at the beginning (6.6°) but it is important to note that these results are based on a sample of ten localised cracks. Thus, for the material studied and the loads applied, a certain discrepancy has been observed between the cracks directions studied on the external surface of the specimen and those studied in the internal sections where it originates. Crack initiation in Mode II direction is not representative of the samples studied in this work.

Additionally, the influence of the hole diameter d on the crack path was analysed. This analysis was based on the ten crack paths for which the crack initiation location was clearly detectable, that is, eight paths for $d = 1.5$ mm and two paths for $d = 3.4$ mm (Appendix C, Table C.3). Unfortunately, there were no clearly detectable crack initiations for $d = 0.8$ mm, so, the analysis was focused only on the other two hole diameters. Regarding the crack initiation angle θ, the average values were $\theta = 4.4°$ and $\theta = 3.7°$ for $d = 1.5$ and 3.4 mm, respectively. The average values for the crack propagation angle θ_1 for crack lengths 1, 5 and 15 averaged grain sizes ($1D$, $5D$ and $15D$) were $\theta_1 = 4.8°$ ($1D$), $\theta_1 = 2.8°$ ($5D$) and $\theta_1 = 1.2°$ ($15D$) for $d = 1.5$ mm, and $\theta_1 = 13.7°$ ($1D$), $\theta_1 = 4.0°$ ($5D$) and $\theta_1 = 1.3°$ ($15D$) for $d = 3.4$ mm. These results indicate that the average values of the angles θ and θ_1 for the two studied diameters are relatively close, with the exception of the value of θ_1 for the first grain ($1D$), whose values are 4.8° and 13.7° for $d = 1.5$ and 3.4 mm, respectively. In any case, the trend of the crack path is basically similar for the two diameters, that is, the crack initiates from a point close to the maximum principal stress point, its direction is close to that of Mode I in the first grains, converging to the Mode I direction as its length increases.

6. Discussion

In this work, a study of the crack directions for S355 steel tubular specimens with a circular hole subjected to cyclic axial loading was carried out. As expected, the cracks started from the circular notch near the point of maximum principal stress. Fracture surface analysis indicated that the cracks initiated from an internal plane and that the crack direction from its initiation was close to the direction perpendicular to the applied load, i.e., in the Mode I direction. A Mode II crack initiation was not observed. The experimental results, although limited to a material and to specific test conditions, are contrary to the usual idea established in the fatigue community that the crack initiates in Mode II and then propagates in Mode I. The theoretical and experimental study of the two stages of fatigue crack growth by Forsyth was mainly carried out for unnotched solids [2]. The presence of a notch, with its effect of generating a stress gradient, might reduce the size of the Mode II initiation stage or even completely inhibit it. Thus, more theoretical and experimental work on notches is needed to determine whether Mode II initiation stage actually occurs or not and which factors influence it.

Table 2
Average and standard deviation (in parentheses) values of crack initiation point angle, θ, and crack direction angles, θ_1.

Path location	θ	θ_1								
		Crack length (a)								
		$1D$	$2D$	$5D$	$10D$	$15D$	$20D$	$L/2$	L	$2L$
External path (Z = 0) (44 cracks from 22 samples)	4.2° (2.7°)	18.4° (16.8°)	11.8° (10.7°)	6.5° (5.9°)	3.7° (4.1°)	2.7° (2.6°)	2.2° (1.9°)	9.4° (8.0°)	6.0° (5.8°)	3.6° (3.8°)
Midplane path Z = −750 μm (44 fracture surfaces from 22 samples)	4.9° (3.7°)	14.2° (15.1°)	9.0° (9.3°)	4.6° (4.0°)	2.5° (2.3°)	1.7° (1.3°)	1.3° (1.2°)	6.9° (7.0°)	4.3° (4.0°)	2.5° (2.4°)
Localised crack initiation paths (10 cracks from 22 samples)	4.3° (2.4°)	6.6° (6.9°)	5.9° (4.2°)	3.1° (1.7°)	1.8° (0.9°)	1.3° (0.8°)	1.0° (0.8°)	5.2° (2.8°)	3.0° (1.7°)	1.9° (1.0°)

The present study can justify the generally good results obtained with fatigue strength and fatigue limit prediction models for notches under cyclic axial loading, such as the Point Method [12] or the N–R model [26–29], which base their predictions on the elastic stresses along a line that begins at the point of maximum principal stress at the notch tip and follows the Mode I direction, not including an initiation line in the Mode II direction. The crack directions obtained experimentally in this work are very close to the Mode I direction even at the very early stages of growth, i.e. a crack length of the order of one grain size. As discussed above, the crack line used in both the Point Method and the N-R model [12,26–29] and the crack line obtained experimentally in this work are very similar. The great similarity between the models' crack line and the experimental crack line is probably one of the reasons for the good predictions provided by these models. The experimental evidence that we provide shows, for the cases under analysis, the absence of the long standing and well accepted Stage I short crack growth propagation along 45° oriented slip bands.

For the case of fatigue endurance prediction for solids with notches under biaxial cyclic loading, current models use different lines to make the prediction, such as the one of the Mode I direction [11], the Mode II direction [12], or the mix-Mode direction [15,30]. This great diversity of crack directions used in current models indicates that it is necessary to extend the studies shown in this work to biaxial loading cases, and also for other materials and notches. The final objective must be to obtain experimental knowledge of the direction of the crack growing from a notch with improved precision, including its initial part. From this knowledge, some modifications of the current fatigue prediction models could be proposed to adjust them as much as possible to the experimental reality. As previously mentioned, the optical technique used in the present work, an optical profilometer with focus variation technology, allows measuring slopes of up to 86° with a resolution of half a micron. The typical slopes of fatigue cracks, supposedly around 45° during initiation and around 0° during propagation, are therefore included in the range of slopes measured by the equipment. The typical average grain size of a metal, at least 15 – 20 μm, is much larger than half a micron resolution, so the microscopical device provides the height of many points per grain. The device meets the technical requirements of this work and the heights shown in the crack paths are very likely close to reality. However, there remains the question of the location of the exact point, or grain, where the crack begins. In the present research, the initiation point was located from the radial lines that point towards the initiation, providing an estimated initiation zone of approximately 50 μm. An average crack path, from the crack paths in parallel planes belonging to the 50 μm initiation zone, was built. The fatigue crack paths presented in this study, which are the average crack paths, are consequently an approximation. Therefore, the crack initiation directions presented in this work are approximate. It is necessary to improve in future work the technique of locating the exact point where the crack initiates if we want to accurately calculate the crack direction in Stage I of crack growth.

7. Conclusions

The results of this work indicate that, for the studied material and test conditions, the fatigue cracks generally initiate from the notch contour and, more specifically, from an internal point and not from the external surface of the specimen. In this internal section, the crack initiation point is placed close to the point of maximum principal stress and the crack direction is close to that of Mode I direction from its beginning. Initiation in Mode II has not been observed. From these results, it can be deduced that the assumption of a Mode I crack from its initiation made by some fatigue prediction models is correct, at least for this material and these test conditions.

In this work, the crack initiation point was located from the radial lines that point towards the initiation, providing an estimated initiation zone of approximately 50 μm. It would be necessary to locate the crack initiation in a more precise way in future work. Despite this, we believe that the results of the crack directions shown in this work represent a certain progress compared to those shown in previously published works, and that they mark a very interesting direction for future research.

Declaration of competing interest

The authors declare that they have no known competing financial interests or personal relationships that could have appeared to influence the work reported in this paper.

Acknowledgements

The authors would like to thank the European Union, the Spanish Government and the Junta de Andalucía for its financial support through grants DPI2017-84788-P and PID2020-117407GB-I00 (FEDER/Ministerio de Ciencia e Innovación - Agencia Estatal de Investigación) and P18-FR-4306 ("Fondo Europeo de Desarrollo Regional (FEDER) y Consejería de Economía, Conocimiento, Empresas y Universidad de la Junta de Andalucía, dentro del Programa Operativo FEDER 2014-2020"). N.O. Larrosa would also like to thank the UK Engineering and Physical Sciences Research Council (EPSRC) for its financial support through grant number EP/S012362/1.

Appendix A

Summary of fatigue test conditions and results for S355 steel ($R = -1$):

(a) Cylindrical smooth specimens:

Test	σ (MPa)	N (cycles)	Remarks
Axial	377	3 900	Failed
	377	6 200	Failed
	345	11 900	Failed
	345	12 000	Failed
	313	82 300	Failed
	313	67 700	Failed
	281	923 400	Failed
	281	1 260 000	Failed
	249	3 500 000	Did not failed
	255	3 500 000	Did not failed
	261	3 500 000	Did not failed
	273	3 500 000	Did not failed
	285	1 078 700	Failed
	273	3 500 000	Did not failed
	285	2 104 000	Failed

(b) Thin-walled tube with a passing through hole of diameter d (mm):

Test	d (mm)	σ (MPa)	N (cycles)	Remarks
Axial	0.80	208	255 200	Failed
		179	964 200	Failed
		150	4 121 800	Failed
		179	641 700	Failed
		208	302 700	Failed
		150	5 000 000	Did not failed
	1.50	197	169 900	Failed
		197	214 100	Failed
		226	78 900	Failed
		226	113 600	Failed
		255	33 000	Failed
		255	29 800	Failed
		182	304 400	Failed
		182	281 500	Failed
		168	5 000 000	Did not failed
		173	415 900	Failed
		168	455 500	Failed
		163	831 100	Failed
		158	876 500	Failed
		153	1 008 100	Failed
	3.40	153	315 600	Failed
		153	491 200	Failed
		240	22 400	Failed
		182	131 800	Failed
		211	52 800	Failed
		182	168 800	Failed
		240	26 800	Failed
		211	49 500	Failed
		124	5 000 000	Did not failed
		134	1 791 900	Failed
		124	3 857 900	Failed
		114	5 000 000	Did not failed
		124	3 133 800	Failed
		114	5 000 000	Did not failed

Appendix B

Experimental crack initiation point angles (θ) for S355 steel ($R = -1$), in absolute value (see Table B.1).

Table B.1
Experimental crack initiation point angles (θ) for S355 steel ($R = -1$), in absolute value.

d (mm)	σ (MPa)	N (cycles)	External crack path $Z = 0$ μm		Midplane path $Z = -750$ μm		Internal crack initiation $Z < 0$ AND $Z \neq -750$ μm	
			θ ($X < 0$)	θ ($X > 0$)	θ ($X < 0$)	θ ($X > 0$)	θ ($X < 0$)	θ ($X > 0$)
0.80	208	255 200	5.3°	2.1°	5.6°	5.7°		
	179	964 200	6.9°	10.8°	4.3°	10.4°		
	150	4 121 800	7.7°	1.9°	5.3°	0.3°		
	179	641 700	2.6°	8.6°	1.9°	11.4°		
	208	302 700	4.7°	12.0°	4.6°	20.3°		
1.50	197	169 900	0.6°	3.4°	6.0°	4.5°		6.1°
								6.8°
	197	214 100	4.6°	0.7°	7.3°	2.5°		
	226	113 600	7.2°	5.5°	8.9°	6.0°		
	182	304 400	3.9°	1.8°	0.0°	2.0°	0.4°	
	182	281 500	3.9°	5.9°	4.7°	4.8°		
	173	415 900	0.7°	5.8°	0.3°	9.0°		6.7°
	168	455 500	6.0°	7.1°	7.3°	8.1°	6.8°	
	163	831 100	5.1°	3.6°	5.1°	5.8°		5.9°
	158	876 500	4.4°	3.2°	7.4°	2.3°		2.7°
	153	1 008 100	3.2°	0.3°	3.8°	1.6°		0.3°
3.40	153	315 600	2.2°	1.9°	2.0°	1.6°	3.1°	
	153	491 200	5.0°	2.6°	4.5°	2.6°	4.3°	
	182	131 800	6.0°	2.1°	8.5°	5.4°		
	182	168 800	2.0°	4.8°	1.2°	1.4°		
	134	1 791 900	4.0°	0.5°	3.2°	0.9°		
	124	3 857 900	2.7°	0.9°	1.6°	1.2°		
	124	3 133 800	9.3°	3.9°	9.3°	4.3°		

Appendix C

Experimental crack direction angles (θ_1) for S355 steel ($R = -1$), in absolute value:
(a) External crack path ($Z = 0$ μm) (see Table C.1).
(b) Midplane thickness crack path ($Z = -750$ μm) (see Table C.2).
(c) Localised internal crack initiation ($Z < 0$ AND $Z \neq 0$ μm) (see Table C.3).

Table C.1
External crack path ($Z = 0$ μm).

d	σ	N	Crack length (a)								
(mm)	(MPa)	(cycles)	$1D$ ($X<0$) ($X>0$)	$2D$ ($X<0$) ($X>0$)	$5D$ ($X<0$) ($X>0$)	$10D$ ($X<0$) ($X>0$)	$15D$ ($X<0$) ($X>0$)	$20D$ ($X<0$) ($X>0$)	$L/2$ ($X<0$) ($X>0$)	L ($X<0$) ($X>0$)	$2L$ ($X<0$) ($X>0$)
0.80	208	255 200	23.7° 0.0°	10.9° 14.6°	8.0° 9.2°	0.8° 4.9°	0.3° 4.1°	0.3° 3.3°	8.2° 25.8°	7.9° 11.7°	0.4° 4.9°
	179	964 200	12.0° Damaged surface	9.3°	0.5°	1.6°	1.3°	0.8°	3.3°	0.2°	1.4°
	150	4 121 800	0.0° 0.9°	1.7° 2.0°	4.5° 2.5°	0.5° 3.1°	1.2° 1.4°	2.4° 1.8°	2.0° 4.5°	0.0° 2.0°	0.9° 0.4°
	179	641 700	53.3° 25.6°	24° 4.5°	8.3° 8.5°	0.3° 4.3°	0.4° 2.8°	0.5° 1.5°	22.0° 14.2°	7.6° 10.4°	0.3° 4.0°
	208	302 700	10.7° 11.2°	8.1° 15.9°	2.4° 7.0°	3.9° 3.4°	2.4° 1.5°	2.2° 2.0°	3.3° 11.2°	0.7° 7.1°	4.0° 3.5°
1.50	197	169 900	52.0° 0.0°	27.3° 15.1°	0.3° 4.0°	13.1° 2.7°	5.0° 0.2°	4.6° 0.0°	8.1° 5.7°	1.6° 5.9°	11.2° 2.9°
	197	214 100	6.6° 44.7°	4.6° 4.9°	2.7° 0.2°	4.6° 0.0°	1.5° 0.7°	1.1° 1.6°	5.4° 8.2°	0.5° 3.4°	4.9° 0.0°
	226	113 600	52.9° 13.9°	39.2° 23.4°	24.7° 27.0°	14.7° 13.9°	6.4° 10.6°	6.3° 7.3°	31.6° 28.7°	28.5° 25.1°	14.7° 13°
	182	304 400	6.1° 15.8°	12.1° 9.1°	9.9° 17.5°	0.6° 9.7°	0.4° 4.9°	0.8° 3.4°	0.5° 11.1°	11.3° 9.7°	1.6° 6.9°
	182	281 500	0.0° 53.0°	8.1° 27.0°	2.0° 9.4°	0.5° 1.0°	0.4° 0.8°	1.0° 0.4°	0.0° 0.0°	2.1° 0.5°	0.6° 0.6°
	173	415 900	6.4° 4.9°	0.5° 3.6°	4.2° 0.2°	2.2° 3.4°	4.8° 3.5°	3.7° 0.1°	0.0° 2.5°	4.2° 0.0°	2.6° 3.4°
	168	455 500	22.1° 14.3°	1.5° 19.4°	5.3° 12.5°	2.9° 4.0°	1.9° 4.5°	2.5° 1.3°	0.0° 17.1°	5.5° 13.9°	2.5° 3.7°
	163	831 100	24.3° 14.1°	8.5° 0.6°	0.0° 2.5°	2.4° 2.2°	1.3° 0.9°	0.2° 1.8°	0.0° 10.0°	1.2° 2.9°	2.2° 2.8°
	158	876 500	9.6° 45.9°	3.3° 18.5°	3.5° 11.5°	0.25° 1.5°	0.5° 0.1°	0.9° 0.4°	4.7° 16.9°	3.4° 8.7°	0.1° 1.4°
	153	1 008 100	17.6° 0.5°	4.9° 29.4°	1.1° 10.6°	3.4° 5.1°	0.5° 1.4°	1.0° 0.4°	4.3° 22.4°	3.1° 8.9°	3.6° 5.1°
3.40	153	315 600	12.0° 0.0°	14.2° 8.7°	3.5° 3.9°	4.4° 1.2°	5.4° 0.1°	4.0° 1.4°	23.7° 7.9°	4.5° 1.8°	4.8° 1.1°
	153	491 200	34.8° 14.4°	23.3° 11.2°	6.8° 5.0°	1.4° 1.7°	0.5° 2.0°	0.6° 0.7°	11.0° 10.0°	10.0° 5.7°	0.8° 1.4°
	182	131 800	26.3° 22.0°	8.8° 15.8°	4.2° 9.4°	9.7° 11.7°	7.0° 8.9°	6.1° 4.5°	10.1° 13.7°	7.5° 10.0°	9.8° 12.7°
	182	168 800	20.4° 17.8°	0.0° 0.0°	13.1° 2.0°	13.7° 3.2°	10.3° 2.4°	4.6° 4.0°	1.1° 0.8°	8.5° 1.4°	11.4° 3.2°
	134	1 791 900	24.8° 25.5°	8.0° 8.3°	1.5° 2.1°	1.3° 1.3°	3.6° 2.2°	4.2° 4.9°	1.5° 5.4°	4.0° 1.3°	2.4° 2.0°
	124	3 857 900	30.9° 22.2°	3.74° 5.7°	0.6° 2.1°	7.2° 1.0°	0.7° 0.7°	5.8° 1.1°	1.5° 2.5°	0.0° 0.0°	6.2° 0.4°
	124	3 133 800	0.0° 3.9°	25.1° 11.9°	10.9° 4.3°	10.0° 0.9°	7.0° 1.9°	4.2° 2.1°	7.2° 10.2°	6.4° 4.2°	10.5° 0.9°

Table C.2
Midplane thickness crack path ($Z = -750\,\mu m$).

d	σ	N	Crack length (a)								
(mm)	(MPa)	(cycles)	$1D$ ($X<0$) ($X>0$)	$2D$ ($X<0$) ($X>0$)	$5D$ ($X<0$) ($X>0$)	$10D$ ($X<0$) ($X>0$)	$15D$ ($X<0$) ($X>0$)	$20D$ ($X<0$) ($X>0$)	$L/2$ ($X<0$) ($X>0$)	L ($X<0$) ($X>0$)	$2L$ ($X<0$) ($X>0$)
0.80	208	255 200	3.7° 6.5°	2.2° 10.9°	3.4° 5.1°	2.2° 6.8°	3.1° 4.1°	2.6° 2.8°	1.9° 7.8°	1.2° 3.7°	2.4° 6.8°
	179	964 200	16.0° 7.3°	3.5° 4.5°	5.3° 10.9°	2.3° 3.6°	1.2° 2.4°	0.4° 1.2°	4.4° 9.8°	6.0° 8.6°	2.3° 3.6°
	150	4 121 800	2.0° 18.7°	1.5° 2.9°	2.8° 0.4°	2.7° 1.1°	0.4° 0.4°	0.3° 0.1°	1.0° 0.4°	3.7° 0.2°	2.8° 1.0°
	179	641 700	0.1° 7.5°	4.9° 15.8°	3.4° 10.0°	1.7° 5.5°	1.1° 2.9°	0.6° 2.7°	4.8° 15.9°	4.4° 10.8°	1.7° 5.6°
	208	302 700	3.9° 0.6°	0.0° 3.9°	1.2° 0.9°	0.4° 2.6°	0.6° 2.5°	1.8° 1.9°	2.8° 0.4°	1.8° 0.2°	0.1° 2.5°
1.50	197	169 900	12.8° 27.4°	5.6° 8.4°	3.4° 0.4°	3.4° 1.3°	1.8° 0.8°	1.1° 0.3°	4.1° 6.9°	3.5° 0.2°	3.6° 1.2°
	197	214 100	5.3° 11.5°	3.6° 5.4°	4.6° 3.9°	2.4° 1.3°	1.6° 0.2°	2.4° 1.0°	3.4° 7.3°	3.5° 2.7°	2.4° 1.1°
	226	113 600	39.9° 14.3°	12.9° 22.0°	1.5° 8.0°	0.7° 3.6°	1.6° 0.8°	2.3° 1.3°	3.4° 15.9°	2.2° 6.7°	1.0° 3.5°
	182	304 400	0.9° 35.1°	8.8° 11.3°	4.7° 6.0°	1.9° 3.9°	0.6° 1.9°	0.7° 0.9°	5.9° 4.3°	4.0° 5.2°	1.9° 3.7°
	182	281 500	4.9° 7.9°	11.1° 5.8°	5.4° 3.8°	0.1° 0.9°	1.1° 1.8°	1.2° 0.0°	3.7° 7.2°	5.3° 4.0°	0.0° 0.6°
	173	415 900	2.7° 8.1°	11.0° 2.5°	6.8° 2.0°	2.5° 0.1°	1.8° 0.6°	1.2° 0.3°	9.7° 1.0°	7.3° 1.1°	2.6° 0.2°
	168	455 500	0.0° 17.5°	2.7° 3.1°	0.7° 2.4°	1.6° 2.3°	1.2° 1.9°	0.4° 1.6°	2.9° 6.1°	0.9° 3.5°	1.7° 2.5°
	163	831 100	9.2° 18.1°	1.0° 1.9°	5.7° 0.8°	3.4° 1.2°	2.1° 0.8°	1.6° 0.2°	12.8° 2.4°	5.1° 1.6°	3.7° 1.2°
	158	876 500	1.1° 0.1°	2.5° 3.7°	5.1° 0.4°	2.3° 0.4°	1.2° 0.3°	0.3° 0.0°	1.9° 0.2°	3.8° 0.3°	2.0° 0.4°
	153	1 008 100	8.0° 3.5°	23.7° 5.7°	9.8° 6.5°	6.3° 3.3°	3.8° 2.1°	2.9° 1.5°	14.2° 2.1°	9.5° 6.4°	6.4° 3.2°
3.40	153	315 600	58.4° 19.6°	26.1° 6.0°	8.8° 4.9°	5.1° 0.5°	3.6° 2.1°	3.0° 2.0°	19.2° 9.8°	7.5° 5.3°	5.0° 0.7°
	153	491 200	21.9° 6.3°	12.1° 3.9°	6.2° 2.5°	4.3° 1.2°	1.4° 1.7°	0.5° 0.8°	8.1° 3.0°	5.3° 1.2°	3.5° 1.1°
	182	131 800	2.8° 24.2°	8.8° 10.5°	8.3° 5.5°	0.6° 1.2°	1.8° 1.5°	0.2° 1.6°	13.1° 5.7°	9.9° 3.2°	0.2° 1.2°
	182	168 800	9.5° 8.3°	29.2° 5.7°	2.2° 1.8°	2.0° 1.1°	1.1° 0.8°	2.9° 2.7°	12.4° 10.9°	1.6° 2.1°	1.9° 1.1°
	134	1 791 900	29.2° 19.7°	0.1° 12.2°	2.0° 3.9°	0.3° 5.2°	0.8° 2.3°	0.2° 1.3°	0.4° 3.1°	1.2° 7.4°	0.3° 6.0°
	124	3 857 900	27.6° 9.9°	12.5° 7.9°	4.5° 1.2°	1.0° 1.1°	1.3° 1.1°	0.7° 0.9°	6.5° 2.8°	4.2° 0.7°	1.2° 1.7°
	124	3 133 800	75.0° 17.6°	51.2° 8.9°	23.5° 0.7°	13.1° 1.1°	7.8° 1.3°	6.0° 0.6°	40.7° 4.8°	23.3° 0.6°	13.1° 1.2°

Table C.3
Localised internal crack initiation ($Z < 0$ AND $Z \neq 0\,\mu m$).

d	σ	N	Crack length (a)								
(mm)	(MPa)	(cycles)	$1D$ ($X<0$) ($X>0$)	$2D$ ($X<0$) ($X>0$)	$5D$ ($X<0$) ($X>0$)	$10D$ ($X<0$) ($X>0$)	$15D$ ($X<0$) ($X>0$)	$20D$ ($X<0$) ($X>0$)	$L/2$ ($X<0$) ($X>0$)	L ($X<0$) ($X>0$)	$2L$ ($X<0$) ($X>0$)
1.50	197	169 900	0.4°	0.1°	0.5°	1.0°	1.3°	1.2°	1.0°	0.9°	1.0°
	197	169 900	9.7°	2.9°	0.3°	2.7°	2.9°	3.0°	1.9°	0.1°	3.5°
	182	304 400	1.8°	6.6°	6.2°	1.9°	1.0°	0.5°	7.3°	6.0°	1.8°
	173	415 900	0.9°	3.0°	2.5°	0.8°	0.2°	0.0°	3.8°	2.8°	0.7°
	168	455 500	4.5°	6.8°	4.4°	3.6°	2.3°	1.5°	6.6°	4.1°	3.6°
	163	831 100	16.6°	12.8°	3.6°	1.5°	0.8°	0.5°	7.1°	3.2°	1.4°
	158	876 500	3.8°	0.5°	3.2°	2.5°	1.4°	0.8°	2.0°	3.5°	2.7°
	153	1 008 100	1.2°	10.3°	2.2°	0.4°	0.2°	0.6°	8.9°	1.8°	0.5°
3.40	153	315 600	21.8°	10.8°	4.7°	1.8°	1.2°	1.2°	8.6°	4.8°	2.0°
	153	491 200	5.6°	5.5°	3.4°	1.8°	1.5°	0.3°	4.3°	3.0°	1.9°

References

[1] Forsyth P. A two stage process of fatigue crack growth. Proceedings of the crack propagation symposium, Vol. 1, 1962, p. 76–94.
[2] Forsyth P. The physical basis of metal fatigue. Blackie and son limited; 1969.
[3] Miller K. A historical perspective of the important parameters of metal fatigue; and problems for the next century. In: Wu X, Wang Z, editors. Proceedings of the seventh international fatigue congress (Fatigue'99). Higher Education Press; 1999, p. 15–39.
[4] Frost NE. Non-propagating cracks in vee-notched specimens subjected to fatigue loading. Aeronaut Q 1957;8(1):1–20.
[5] Frost NE. Notch effects and the critical alternating stress requiered to propagate a crack in an aluminium alloy subject to fatigue loading. J Mech Eng Sci 1960;2(2):109–19.
[6] Meneghetti G, Susmel L, Tovo R. High-cycle fatigue crack paths in specimens having different stress concentration features. Eng Fail Anal 2007;14(4):656–72.
[7] Tanaka K, Morita K, Akiniwa Y. Fatigue thresholds of holed components under in-phase and out-of-phase torsional and axial loadings. Fatigue Fract Eng Mater Struct 2008;31(12):1079–90. http://dx.doi.org/10.1111/j.1460-2695.2008.01298.x.
[8] Berto F, Lazzarin P, Yates JR. Multiaxial fatigue of V-notched steel specimens: a non-conventional application of the local energy method. Fatigue Fract Eng Mater Struct 2011;34(11):921–43. http://dx.doi.org/10.1111/j.1460-2695.2011.01585.x.
[9] Gates N, Fatemi A. Notched fatigue behavior and stress analysis under multiaxial states of stress. Int J Fatigue 2014;67:2–14. http://dx.doi.org/10.1016/j.ijfatigue.2014.01.014.
[10] Lorenzino P, Navarro A. Growth of very long "short cracks" initiated at holes. Int J Fatigue 2015;71:64–74. http://dx.doi.org/10.1016/j.ijfatigue.2014.03.023.
[11] Susmel L. Multiaxial notch fatigue: from nominal to local stress/strain quantities. Woodhead Publishing; 2009.
[12] Taylor D. The theory of critical distances: a new perspective in fracture mechanics. Elsevier Science; 2010.
[13] Vantadori S, Carpinteri A, Fortese G, Ronchei C, Scorza D, Zanichelli A. Fatigue lifetime evaluation of notched components: Implementation of the control volume concept in a strain-based LCF criterion. Theor Appl Fract Mech 2018;97:400–8. http://dx.doi.org/10.1016/j.tafmec.2017.07.001.
[14] Navarro A, Vallellano C, Chaves V, Madrigal C. A microstructural model for biaxial fatigue conditions. Int J Fatigue 2011;33(8):1048–54. http://dx.doi.org/10.1016/j.ijfatigue.2010.11.001.
[15] Chaves V, Navarro A, Beretta G, Madrigal C. Microstructural model for predicting high cycle fatigue strength in the presence of holes under proportional biaxial loading. Theor Appl Fract Mech 2014;73:27–38. http://dx.doi.org/10.1016/j.tafmec.2014.08.001.
[16] Chaves V, Beretta G, Navarro A. Biaxial fatigue limits and crack directions for stainless steel specimens with circular holes. Eng Fract Mech 2017;174:139–54. http://dx.doi.org/10.1016/j.engfracmech.2016.11.022.
[17] Chaves V, Beretta G, Balbín JA, Navarro A. Fatigue life and crack growth direction in 7075-T6 aluminium alloy specimens with a circular hole under biaxial loading. Int J Fatigue 2019;125:222–36. http://dx.doi.org/10.1016/j.ijfatigue.2019.03.031.
[18] Chaves V. Ecological criteria for the selection of materials in fatigue. Fatigue Fract Eng Mater Struct 2014;37(9):1034–42. http://dx.doi.org/10.1111/ffe.12181.
[19] Timoshenko S, Goodier J. Theory of elasticity (international student edition). Engineering societies monographs, 3rd ed.. McGraw-Hill; 1982.
[20] Beretta G. Fatiga en componentes con concentradores de tensión bajo carga biaxial. (Ph.D. thesis), Universidad de Sevilla (Spain); 2016, 2016.
[21] ASTM. ASTM E739-91 standard practice for statistical analysis of linear or linearized stress-life ($S-N$) and strain-life ($\epsilon-N$) fatigue data. ASTM International; 2004.
[22] Haddad MHE, Topper TH, Smith KN. Prediction of non propagating cracks. Eng Fract Mech 1979;11(3):573–84. http://dx.doi.org/10.1016/0013-7944(79)90081-X.
[23] Chaves V, Navarro A. Application of a microstructural model for predicting notch fatigue limits under mode I loading. Int J Fatigue 2009;31(5):943–51. http://dx.doi.org/10.1016/j.ijfatigue.2008.09.009.
[24] Navarro A, Vallellano C, de los Rios ER, Xin XJ. Notch sensitivity and size effects described by a short crack propagation model. In: Beynon JH, Brown MW, Smith RA, Lindley TC, Tomkins B, editors. Engineering against fatigue. Balkema Publishers; 1997, p. 63–72.
[25] ANSYS. ANSYS mechanical APDL, release 18.0. Help System.
[26] Larrosa NO, Navarro A, Chaves V. Calculating fatigue limits of notched components of arbitrary size and shape with cracks growing in mode I. Int J Fatigue 2015;74:142–55. http://dx.doi.org/10.1016/j.ijfatigue.2015.01.002.
[27] Larrosa NO, Chaves V, Navarro A, Ainsworth RA. Application of the Microstructural Finite Element Alternating Method to assess the impact of specimen size and distributions of contact/residual stress fields on fatigue strength. Comput Struct 2017;179:15–26. http://dx.doi.org/10.1016/j.compstruc.2016.10.011.
[28] Balbín JA, Chaves V, Larrosa NO. Pit to crack transition and corrosion fatigue lifetime reduction estimations by means of a short crack microstructural model. Corros Sci 2021;180:109171. http://dx.doi.org/10.1016/j.corsci.2020.109171.
[29] Chaves V. A simplified Navarro-Rios model to predict fatigue limits in notched components.. Int J Fatigue 2021;149:106264. http://dx.doi.org/10.1016/j.ijfatigue.2021.106264.
[30] Carpinteri A, Spagnoli A, Vantadori S, Viappiani D. A multiaxial criterion for notch high-cycle fatigue using a critical-point method. Eng Fract Mech 2008;75(7):1864–74. http://dx.doi.org/10.1016/j.engfracmech.2006.11.002.